Holistic Seismic Monitoring of CCS with Active and Passive Data: A synthetic feasibility study based on Pelican site, Australia

Mrinal Sinha[1,2], Erdinc Saygin[1,2], Andrew S. Ross[2], Ludovic Ricard[2]

[1]CSIRO Deep Earth Imaging FSP
[2]CSIRO Energy

Key Points:

- Multifaceted monitoring of a modelled CO_2 plume using passive and active synthetics based on an offshore CO_2 sequestration site in Australia
- Shows distributed acoustic sensing (DAS) based passive seismic imaging combined with wave equation inversion methods can cost-effectively monitor carbon capture and storage (CCS)

Corresponding author: Mrinal Sinha, mrinal.sinha@csiro.au

Abstract

Carbon capture and storage (CCS) is forecast to play a significant role towards CO_2 emissions reduction. Cost-effective and simplified monitoring will be essential for rapid adoption and growth of CCS. Seismic imaging methods are regularly utilized to monitor low-velocity anomalies generated by injection of CO_2 in the subsurface. In this study we generate active and passive synthetic seismic datasets at different stages of CO_2 injection in the subsurface based on geologically constrained subsurface models of the Pelican storage site in the Gippsland Basin, Australia. We apply full waveform inversion (FWI) and wave-equation dispersion (WD) inversion to seafloor deployed distributed acoustic sensing (DAS) data to reconstruct the low-velocity anomalies. We model both strain (DAS) and displacement datasets for the active data component of the study and show that they result in similar reconstruction of the CO_2 anomaly. FWI based time-lapse imaging of active data yields the most accurate results. However, this approach is expensive and also suffers from complex issues because of the near-onshore location of the storage site. Alternatively inverting passive data results in only minor differences, but can still effectively monitor changes in the subsurface, and assist in monitoring the CO_2 plume at the reservoir depth. Furthermore, we demonstrate the capability of WD for inverting Scholte-waves derived from ambient noise for shallow detection of CO_2 in the unlikely event of a leakage. Therefore, we propose a mixed mode monitoring strategy where passive data is utilised for routine monitoring while active surveys are deployed only when further investigation is required.

Plain Language Summary

Carbon capture and storage has been identified as a key technology to combat climate change. The Pelican field in the Gippsland Basin, Australia has been identified as a potential storage site for CCS. Cost-effcient, high fidelity, low impact monitoring of the CO_2 plume would be essential for satisfying the regulations relating to measuring, monitoring and verification of CO_2 storage. In this desktop study we use subsurface models representative of the Pelican field to synthesize active and passive datasets. To make the seismic monitoring more cost-effcient, high fidelity and low impact we explore the use of distributed acoustic sensing (DAS) over conventional seismic sensors in this offshore setting. We then use seismic imaging techniques to study the limits of these methods to monitor the evolution of CO_2 plume stored underground as subsequent injections take place. Our findings show that application of state of the art seismic imaging techniques to passive and active datasets, in a multifaceted fashion can optimize the costs and environmental footprint associated with monitoring of CO_2 storage.

1 Introduction

Carbon capture and storage (CCS) has been identified as a key contributor towards mitigation of climate change and the achievement of the net zero goal by 2050 (IEA, 2021). CCS refer to the technologies that involve the capture of CO_2 from the environment or industrial emissions, followed by the storage of the captured CO_2 at a secure and long-lasting storage site. Under the CarbonNet project, the Pelican site in the Gippsland Basin has been identified as a potential storage site (Hoffman, 2018) in Australia.

Long-term monitoring of CO_2 storage is crucial for safety and regulatory purposes and therefore is essential for a functional CCS project (Glubokovskikh et al., 2016; Urosevic et al., 2011; Jenkins et al., 2015). A successful monitoring program is needed to ensure conformance and containment of the injected CO_2 in the reservoir (Harvey et al., 2022). For subsurface CO_2 geological storage in offshore settings 4D timelapse seismic survey have been used for CO_2 plume imaging and monitoring (Furre et al., 2017). Conventional 4D Marine control source seismic surveys with towed systems or ocean bottom nodes combined with full-waveform inversion (FWI) technology provide highly-resolved

images of the Earth's subsurface. This technology's efficacy has been successfully demonstrated on various CCS projects like Sleipner (Chadwick & Noy, 2015). Although conventional 4D seismic is capable of producing very accurate results it can be expensive, environmentally intrusive and poses a logistically complex challenge as the Pelican site lies in an off-shore/onshore transition zone.

More recently there have been rapid advancements in seismic acquisition using fibre-optic based sensors, also known as distributed acoustic sensing (DAS). DAS systems are a cost-efficient way of deploying a permanent reservoir monitoring (PRM) system for long term monitoring. DAS measures the strain/strain-rate measurement along the length of the fibre averaged over a gauge length (Ajo-Franklin et al., 2019). It is capable of producing broadband measurements that are densely sampled data in space and time, thereby creating large volumes of data (Lindsey et al., 2017). Active surveys only make measurements during a limited period of time but progress has been made towards continuously exciting sources combined with DAS as a recording system, which results in a truly permanent reservoir monitoring system (Tsuji et al., 2021). DAS can also be utilized to record passive seismic data which consists primarily of oceanic waves, anthropogenic sources (traffic noise, etc.) and microseismic events. Virtual active data can be generated by applying ambient noise processing workflows (Bensen et al., 2007) to the passive data. These virtual data are usually rich in surface waves, which can be inverted to obtain a shallow shear-wave velocity model.

In this work, we use wave-equation based inversion methods for imaging the simulated CO_2 plume. These methods perform well when the data is rich in low-frequency content and has dense raypath coverage. Availability of low-frequencies in broadband DAS data can mitigate cycle-skipping and the requirement of an accurate starting model can be relaxed. Additionally, densely spaced DAS sensors provide increased raypath coverage which can improve the image-resolution and makes the inversion well-conditioned. Therefore, wave-equation inversion methods in theory should combine very well with off-shore DAS to produce high-quality subsurface images.

2 Methodology

2.1 Full Waveform Inversion for Time-Lapse Imaging

FWI has been used extensively to invert highly-resolved earth models from seismic data. In its naive implementation, it seeks out the subsurface model $\mathbf{m}$ which minimizes the L_2 norm misfit between the observed d^{obs} and the predicted data $d(\mathbf{m})^{pred}$

$$J(\mathbf{m}) = \frac{1}{2}\sum \left(d(\mathbf{m})^{pred} - d^{obs}\right)^2. \tag{1}$$

FWI implementation and gradient derivation for conventional data recordings such as displacement data are well known (Tarantola, 1986; Mora, 1987). When it comes to DAS data which is a strain based measurement the formulation of FWI needs to be adapted to account for strain which is essentially the gradient of the displacement field.

We simplify the DAS data to strain measuring point sensors and ignore the averaging effect over gauge length. A spectral-element based modelling engine Salvus was used for forward and inverse simulations . Isotropic wave equation shown below was used for forward modelling (Afanasiev et al., 2018)

$$\rho(\mathbf{x})\frac{\delta^2\mathbf{u}(x,t)}{\delta t^2} - \nabla.(2\mu(\mathbf{x})\epsilon(\mathbf{u}(\mathbf{x},\mathbf{t})) + \lambda(\mathbf{x})(\nabla.\mathbf{u}(\mathbf{x},t))I) = f(\mathbf{x},t), \tag{2}$$

where u and $\epsilon(\mathbf{u})$ are the displacement vector and strain tensor fields, respectively and λ and μ are the Lamé parameters. DAS cables acquires the projected component of the strain sensor along the tangent-direction of the optical fiber given by ϵ_{tt}. Eaid et al. (2020)

expressed the mathematical relationship as shown here:

$$\epsilon_{tt}(s) = (\hat{\mathbf{e}} \cdot \hat{\mathbf{x}})^2 \epsilon_{xx} + (\hat{\mathbf{e}} \cdot \hat{\mathbf{y}})^2 \epsilon_{yy} + (\hat{\mathbf{e}} \cdot \hat{\mathbf{z}})^2 \epsilon_{zz} + 2(\hat{\mathbf{e}} \cdot \hat{\mathbf{x}})(\hat{\mathbf{e}} \cdot \hat{\mathbf{y}}) \epsilon_{xy} + 2(\hat{\mathbf{e}} \cdot \hat{\mathbf{x}})(\hat{\mathbf{e}} \cdot \hat{\mathbf{z}}) \epsilon_{xz} + 2(\hat{\mathbf{e}} \cdot \hat{\mathbf{y}})(\hat{\mathbf{e}} \cdot \hat{\mathbf{z}}) \epsilon_{yz}. \tag{3}$$

In this equation $\hat{\mathbf{e}}(s)$ is the unit vector tangent to the fibre at s and $\hat{x}$, $\hat{y}$, $\hat{z}$ are unit vectors along the orthogonal axes of a Cartesian coordinate system. For a horizontal fibre oriented along the $\hat{\mathbf{x}}$ direction would result in a tangent vector $\hat{\mathbf{e}} = \hat{\mathbf{x}}$ for all s along the fibre, which implies that ϵ_{xx} is effectively recorded at the DAS cables.

The optimization problem in equation 1 is solved using gradient-based methods (Nocedal & Wright, 2006). This is done by estimating the Frechét derivatives for different model parameters using the adjoint state method (Plessix, 2006). As the predicted and observed data in the DAS case is the tangential component (ϵ_{tt}) of the strain tensor, the back-propagated adjoint source needs modification. This adjoint source is a moment tensor source given by Yust et al. (2023) as

$$({\epsilon_{tt}}^{pred} - {\epsilon_{tt}}^{obs}) \hat{e} \hat{e}^T. \tag{4}$$

For a DAS cable lying on a flat seabed oriented along the $\hat{x}$ direction the adjoint source from equation 4 simplifies to a moment tensor source with M_{xx} being the only non-zero component, with $M_{xx} = {\epsilon_{xx}}^{pred} - {\epsilon_{xx}}^{obs}$.

Time-lapse imaging relies on imaging of datasets (two-sets) acquired at different stages of monitoring. Conventional time-lapse change can be evaluated by differencing the inverted models from the baseline and monitor datasets. Gradient based methods provide local minima as solutions, this can introduce uncertainties in time-lapse estimation due to the sensitivity of FWI convergence to starting models. This may lead to spurious time-lapse changes arising from convergence of the two inversions to unsuitable local minimas. A joint inversion alternative to conventional time-lapse inversion is the double-difference waveform inversion strategy proposed by Yang et al. (2016) to mitigate this issue. This is a two-stage strategy which begins by inverting

- the baseline dataset to invert baseline subsurface model $\mathbf{m_{base}}$

$$J(\mathbf{m_{base}}) = \frac{1}{2} \sum \left(d_{base}^{pred}(\mathbf{m_{base}}) - d_{base}^{obs}\right)^2, \tag{5}$$

  where d_{base}^{obs} and d_{base}^{pred} are observed and predicted baseline datasets, respectively.
- The inverted baseline model $\mathbf{m_{base}}$ is chosen as the initial model for minimizing a double-difference misfit to invert for baseline model $\mathbf{m_{mon}}$ given as

$$J(\mathbf{m_{mon}}) = \frac{1}{2} \sum \left((d_{mon}^{pred}(\mathbf{m_{mon}}) - d_{mon}^{obs}) - (d_{base}^{pred}(\mathbf{m_{base}}) - d_{base}^{obs})\right)^2, \tag{6}$$

  the two newly introduced data variables are observed (d_{mon}^{obs}) and predicted (d_{mon}^{pred}) monitor datasets. Alternatively, this misfit can be interpreted as a difference between the observed and predicted time-lapse data difference.

This approach is limited by the need for good repeatability between the two datasets. The method requires that the illumination from the raypaths remain the same, which is possible for active seismic surveys with carefully chosen source and receiver locations. However, this condition is rarely satisfied for natural events like microseismic events and earthquakes.

2.2 Wave-Equation Inversion of Passive Seismic Waves for Near Surface Imaging

In an offshore setting Scholte waves are generated at the water-sediment interface (seafloor) and these are dispersive in nature. This characteristic of Scholte-waves can be

exploited to reveal the shallow S-wave velocity model of the shallow subsurface underneath the seafloor. Williams et al. (2021) utilize the dispersion curves obtained from ambient noise crosscorrelations to invert a 1D S-wave velocity structure using phase velocity inversion at different locations. Alternatively, Chen and Saygin (2022) used the wave-equation based WD method described below to generate 2D shear-wave velocity images and interpolated them to construct a 3D velocity model.

In the absence of low-frequencies and sufficiently accurate starting models the inversion can easily converge to a cycle-skipped local minima. A skeletonized attribute of seismic data is the dispersion curve extracted from the shot-gathers containing dispersive interface waves (surface and guided waves). Li et al. (2016) devised an optimization problem which searches for the best shear-wave velocity model by matching the observed and predicted dispersion curves, depicted as κ in the equation below

$$J(\mathbf{m}) = \frac{1}{2}\sum \left({\kappa_\omega}^{obs} - \kappa_\omega(\mathbf{m})^{pred}\right)^2, \tag{7}$$

where ${\kappa_\omega}^{obs}$ and ${\kappa_\omega}^{pred}$ are the dispersion curves extracted form the observed and predicted data, respectively through a τ-p transform.

Using a simplified version of the data, dispersion curves, results in a smoother misfit surface, which makes the inversion process more robust, and it also avoids the simplified layered media assumptions of convention dispersion-curve inversion methods. We use WD method for inverting ambient noise crosscorrelations derived for simulated passive data recorded by DAS fibres. The underlying equations for the calculating the gradients using a connective function approach are given in Liu et al. (2022).

3 Numerical Examples

All numerical examples are based on velocity models derived from 3D seismic survey in the Pelican field. The Vp velocity model was derived from the active seismic survey Pelican 3D MSS (CarbonNet) 2018, the shear-wave velocity model was established using the $\frac{V_p}{V_s}$ ratio from well-logs in the area. The density values in non-water part of the model kg/m^3 were derived from the P-wave velocity model in m/s using the Gardner's relationship

$$\rho = 1000 \times (0.31 \times {V_p}^{0.25}). \tag{8}$$

3.1 Simulated 2D Active Reservoir Monitoring

The observed datasets were simulated for 21 shots placed evenly every 500 m between 5 km and 15 km. These were recorded by 20 km long DAS cable lying on the seafloor corresponds to 4001 sensors spaced at an interval of 5 m. DAS cable is oriented along x-direction, so it records the ϵ_{xx} component of the strain tensor. We also record the simulated data on conventional sensors recording u_x component of the displacement vector field for comparison. All models are 20.8 km long in x-direction with a maximum depth of 5.5 km. 2D isotropic elastic wave equation was modelled using spectral element method for mesh sizes supporting a maximum frequency of 9 Hz. Figure 1 shows the acquisition setup superimposed on the baseline and monitor velocity models. Initial injection of CO_2 leads to a 10% drop in V_p for the baseline survey, followed by further injection causes increased saturation of CO_2 in existing areas results in further decrease in acoustic impedance, but also leads to migration of the CO_2 plume to newer areas of the reservoir as depicted by the difference of the monitor and baseline velocity models depicted in Figures 2 (a-b).

Initial model used for baseline FWI is the same as pre-injection FWI model shown in Figure 2a. As the baseline and monitor survey acquisition parameters remaining unchanged implies excellent repeatability, so we use the double-difference approach for estimating the time-lapse change through FWI. The inverted baseline anomaly and the

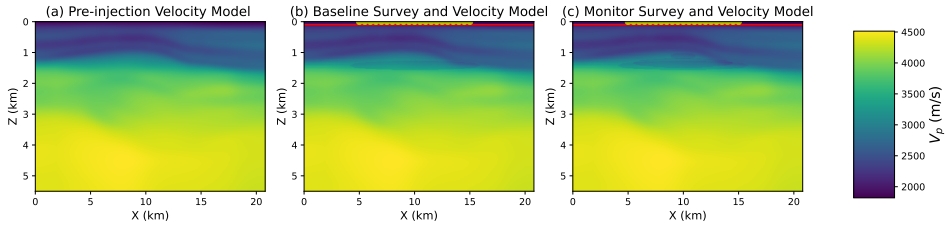

Figure 1. (a) Pre-injection velocity model and initial velocity model for baseline FWI. Velocity models and acquisition setup for the (b) baseline and (c) monitor surveys. The red line here denotes the DAS cable spread out on the seafloor and the yellow trapezoids are the 21 active sources used for the experiment.

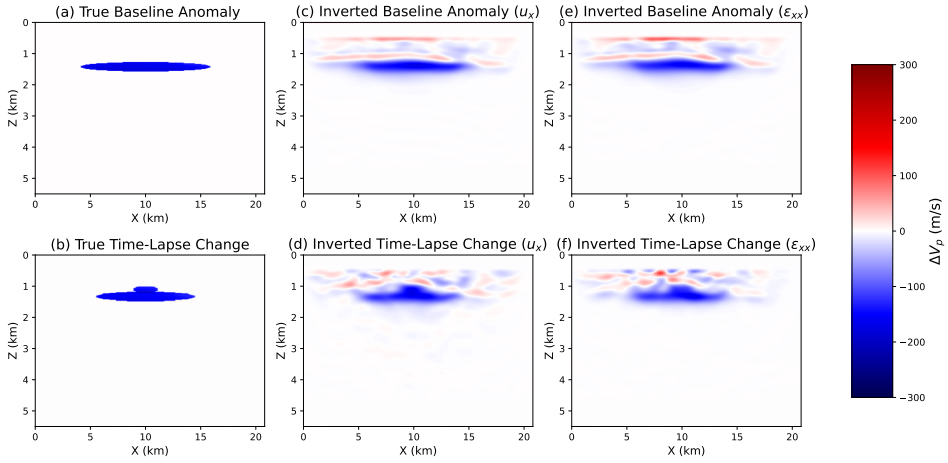

Figure 2. Anomalies introduced by addition of CO_2: true (a) baseline anomaly(difference between the baseline and pre-injection velocities) (b) true time-lapse change (difference between monitor and baseline velocities). Inverted baseline and time-lapse results for u_x data (c-d) and DAS data (e-f).

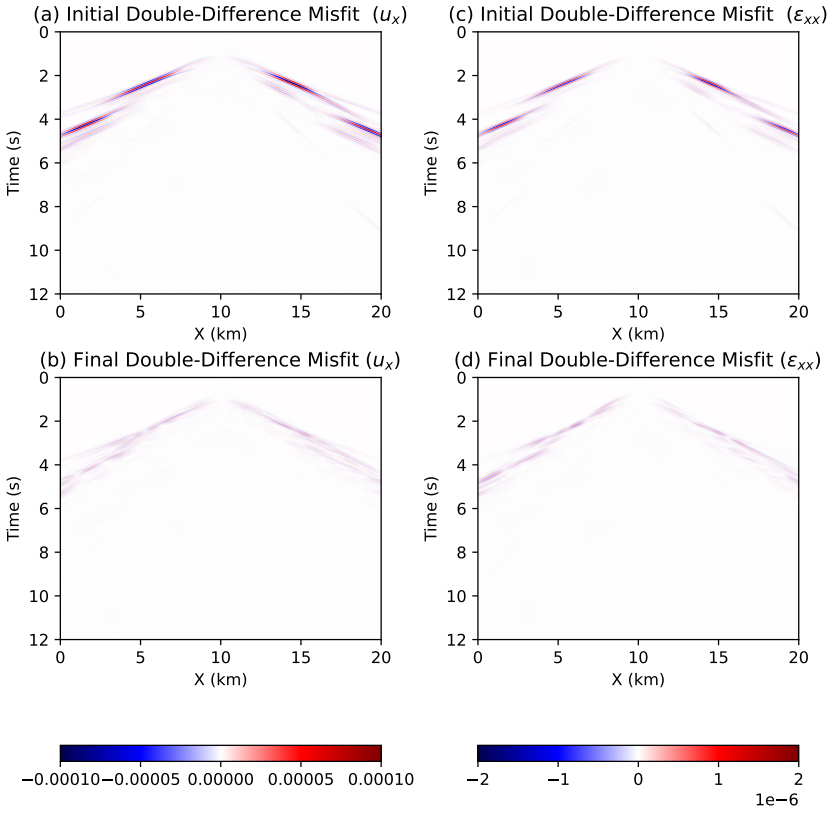

Figure 3. Double-difference displacement misfit at the (a) initial and (b) final iterations of the time-lapse inversion for u_x data. Double-difference DAS misfit at the (c) initial and (d) final iterations of the time-lapse inversion.

time-lapse change derived from u_x and DAS data are shown in Figures 2 (c-d) and Figures 2 (e-f), respectively. The results are in good agreement with each other, and therefore establishes the suitability of surface DAS cables as an alternative to conventional OBN sensors as a monitoring tool.

Figures 3 (a-b) and 3 (c-d) show the evolution of double-difference misfits (shot in the center of the domain) for u_x and the DAS data, respectively. Final iteration misfits for both datasets are much reduced from the initial point and majority of the model updates are driven by the intermediate and wide-angled reflections in the data. The DAS data for the recorded P-waves, suffer from an obliquity factor of $\cos^2\theta$ which is stronger than that of the horizontal component u_x by a factor of $\cos\theta$ (Lindsey & Martin, 2021), therefore minimum angle threshold for a meaningful update is slightly greater for DAS data.

3.2 Wave Equation Inversion of Simulated Passive DAS Data

The synthetic passive dataset consists of 50 ambient-noise recordings, each being 30 seconds long. The ambient noise records were synthesized using 3D isotropic elastic modelling with 10,000 randomly located sources which are excited with random time-delays for a maximum frequency of 3 Hz. These ambient noise records are recorded by a single 15 km long DAS cable lying on the flat sea-floor. The map view of the acquisition setup is depicted in Figure 4a. Even though a leakage is unlikely, to test the mon-

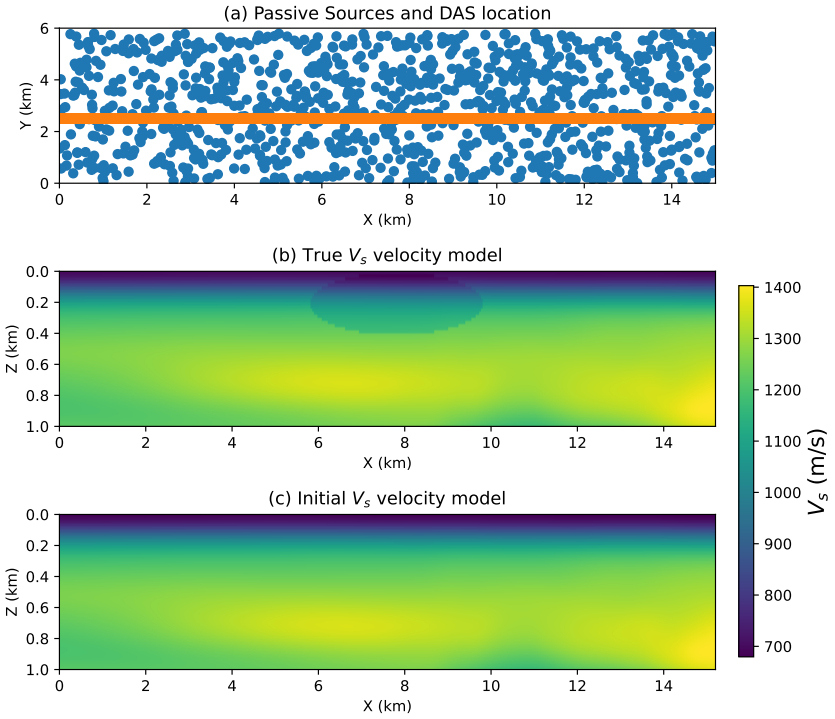

Figure 4. (a) Plan view of the ambient noise source and DAS cable. The orange line is the seafloor DAS cable and the blue dots represent the source locations.(b) The true V_s velocity model with the CO_2 leakage anomaly and (c) pre-leakage V_s velocity model (also the initial model for inversion).

itoring systems ability to detect CO_2 in shallow subsurface intervals we simulate a low-velocity leakage anomaly of 5% as shown in Figure 4b. The model size is 15.2 km long and 1 km deep in x and z directions, respectively with a grid spacing of 20 m.

DAS records were crosscorrelated and then followed by normalization and stacking, with a 50% overlap between the ambient noise records. 350 virtual shot gathers (VSGs) are synthesized using the aforementioned workflow for WD inversion spaced at an interval of 40 m with a modified receiver spacing of 20 m. An example ambient noise record and a VSG are shown in Figures 5a and 5b, respectively. The VSG is able to reconstruct the Scholte waves fairly well, and the dispersive nature of these surface waves can be exploited by WD method.

The dispersion curves extracted from these VSGs serve as the observed dispersion curve in equation 7. The pre-leakage model without the low-velocity anomaly shown in Figure 4b is used as the initial model for WD inversion. After 25 iterations of WD we arrive at a model which best matches the observed dispersion curve obtained from the VSGs. The true CO_2 anomaly and the recovered CO_2 perturbation by WD method are shown in Figure 6. The CO_2 anomaly is roughly reconstructed in the correct location but it fades with depth due to the limited depth sensitivity of Scholte waves at this frequency band.

For quality control purposes, we examine the convergence in the dispersion curve domain. The dispersion curves were obtained by applying Radon transform to the Fourier transformed VSG. We only show frequency greater than 0.9 Hz portion of the dispersion curve for inversion, as the observed dispersion curve below this threshold was noisy

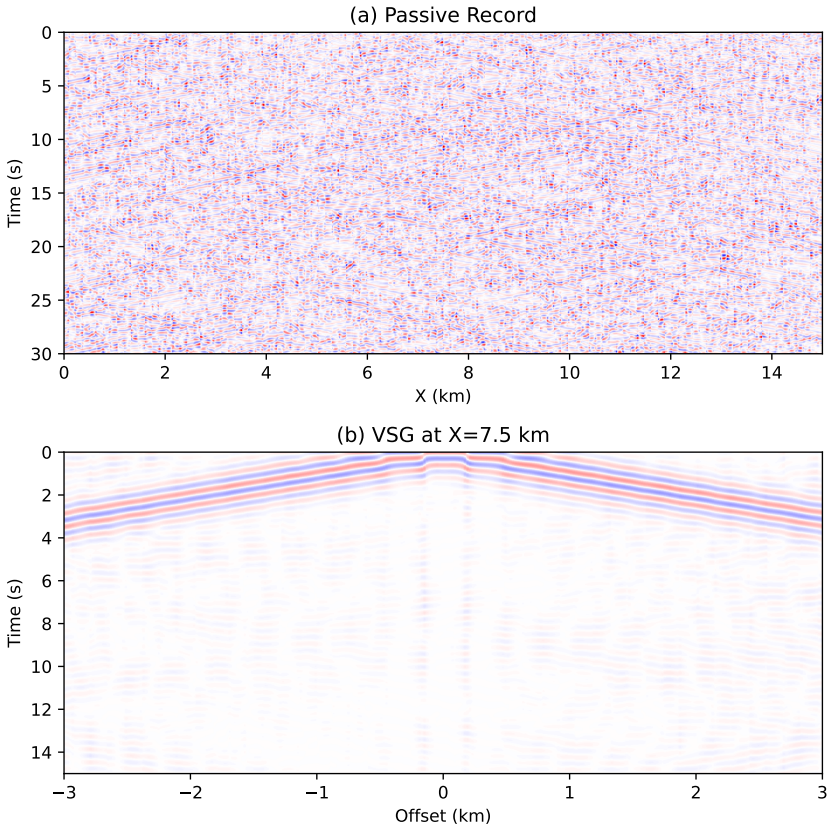

Figure 5. (a) Ambient noise record and the synthesized (b) virtual shot gather (VSG).

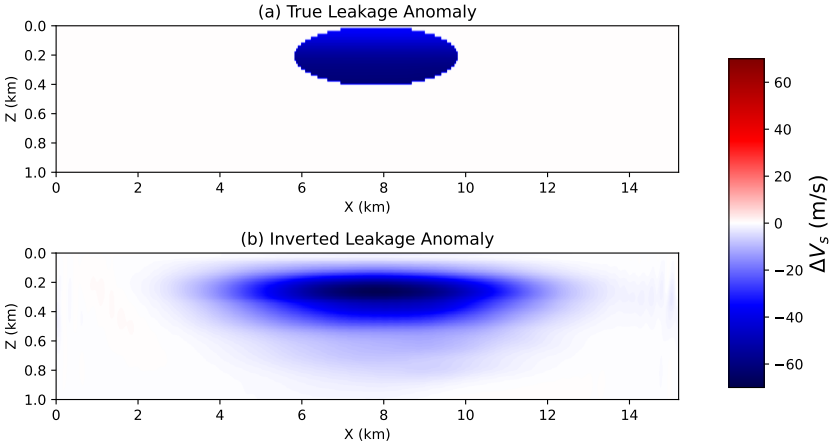

Figure 6. (a) True CO_2 leakage anomaly and (b) the recovered anomaly after 25 iterations of WD method.

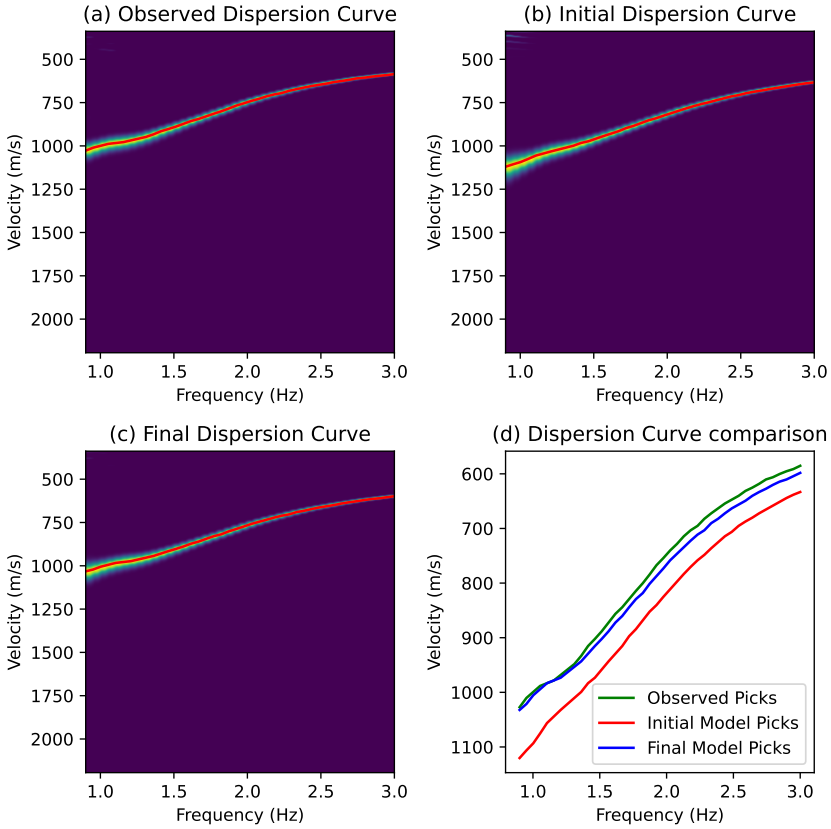

Figure 7. (a) Observed dispersion curve and picks (red) from the VSG shown in Figure 5. Dispersion curves and picks (red) from modelled elastic shots using the (b)initial and (c) final models, respectively. (d) Dispersion curve comparison of the picked dispersion curves shows the convergence of the model.

leading to spurious picks. The observed dispersion curve picks derived from the VSG and the initial model-based dispersion curve picks in Figures 7a and Figures 7b are shown in green and red colours in the Figure 7d. Figure 7d illustrates that the effect of injecting CO_2 has been captured in the dispersion curve domain effectively. The final dispersion curve estimated from the WD inversion result (shown in blue) matches the observed dispersion curve fairly well. This establishes that WD has converged to a suitable local minima in the dispersion curve domain.

More importantly, this implies that the dispersion curve comparisons extracted from ambient noise cross-correlations derived from pre-leakage and post-leakage scenarios can aid in early detection of shallow leakages. A drop in shear wave velocity caused by leakage of shallow CO_2 could be substantial enough to cause a shift in the dispersion curve domain. On establishing this translation of dispersion curve towards lower velocities from the baseline curve, a more thorough inversion based investigation can be launched for imaging the simulated subsurface leakage spatially.

3.3 Time-Lapse FWI with Simulated Microseismic and Earthquake Events

In this section we demonstrate the usage of earthquake and microseismic events for monitoring the CO_2 plume within the reservoir in the subsurface. The model domain is 20.8 km and 8 km long in x and y directions, respectively with a maximum depth of

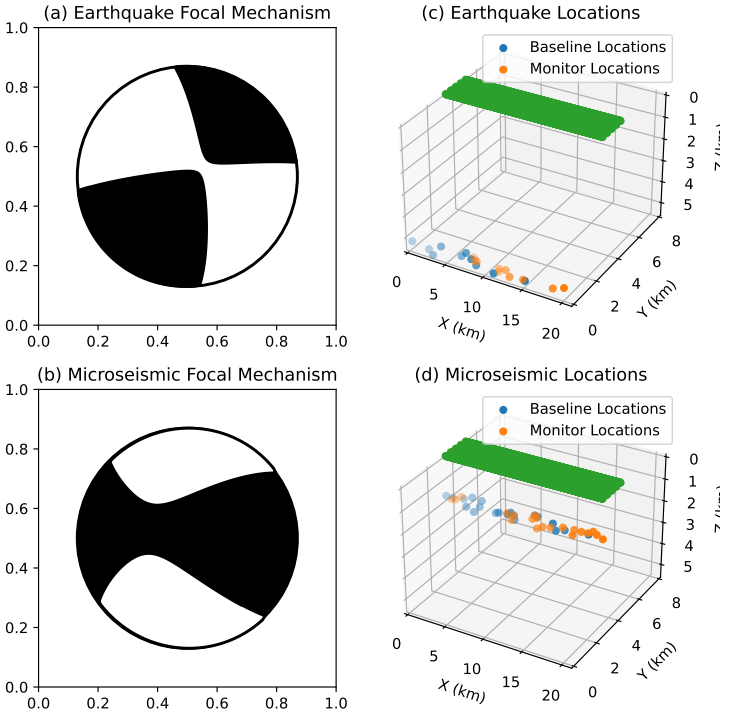

Figure 8. Focal mechanisms for (a) earthquake and (b) microseismic sources. Baseline (blue) and monitor (orange) source locations for (c) earthquake and (d) microseismic events. DAS cables on the seabed are shown in green.

5.5 km. 10 earthquake and 20 microseismic events were simulated for the synthetic experiment. Figures 8c and 8d show the baseline (in blue) and monitor (in orange) events for earthquakes and microseismics, respectively. Earthquake and microseismic event source location are chosen randomly with different random locations for the baseline and monitor inversions, implying that the time-lapse setup suffers from poor repeatability unlike the case of active experiment discussed previously. The earthquake and microseismic datasets were simulated for record lengths of 6 s and 10 s, respectively. The maximum frequency for these elastic simulations was limited to 4 Hz. The source mechanism for the microseismic events are a combination of a dominant double-couple (DC) with a compensated linear vector dipole (CLVD) and an isotropic component (Kamei et al., 2015). For the earthquake events we use the focal mechanism of the Mw 5.9 Woods Point Earthquake, the strongest earthquake recorded in the state of Victoria since the availability of modern seismic instrumentation (Hoult et al., 2021). The base focal mechanism for the modelled earthquakes and microseismic sources are shown in Figures 8a and 8b, respectively.

The monitoring setup consists of 5 horizontal DAS cables (Figure 8(c-d) in green) oriented along the x-axis spaced at an interval of 200 m in y-direction, where each DAS cable consists of 800 channels spread at an interval of 20 m recording the ϵ_{xx} component of the strain field. This has been done to capture the 3D nature of the seismic wavefield and thus aid in more accurate monitoring of the plume as opposed to a single cable utilized in previous experiments.

2D slices of the 3D velocity models are shown in Figure 9, where the leftmost column shows the pre-injection model (initial model for FWI), followed by the velocity mod-

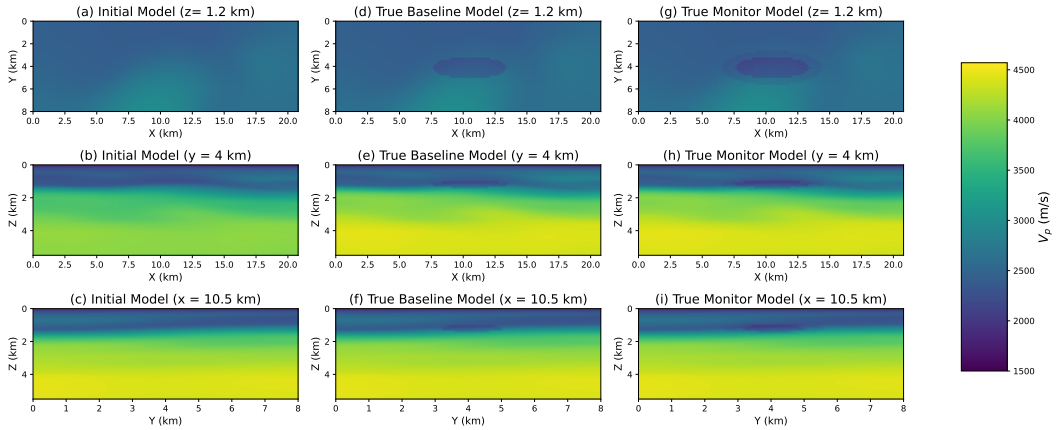

Figure 9. 2D slices of the (a-c) pre-injection velocity model and (d-f) baseline and (g-i) monitor P-wave velocity models.

els used for generating the baseline and monitor datasets in the center and the rightmost columns, respectively. As shown previously, introduction of CO_2 leads to a drop in V_p values for both the baseline and monitor injections.

The perturbation caused by CO_2 baseline injection is emphasized in Figure 10 (a-c), which is the difference between baseline (Figure 9 (d-f)) and pre-injection (Figure 9 (a-c)) velocity models. The ground-truth for the time-lapse change is shown in Figures 11 (a-c), and it is equivalent to the difference between the monitor (Figure 9 (g-i)) and baseline velocity models (Figure 9 (d-f)).

The earthquake locations are clustered at the edge of the model, we have chosen the deepest allowable depths for the model ranging from 5 to 5.5 km. The magnitudes of the simulated earthquakes vary between 2 to 4. In practice, natural earthquakes occurring in a chosen time-interval after the baseline and monitor injections take place. Conventional L2-norm FWI was used for inverting both baseline anomaly and time-lapse changes. As the repeatability suffers from varying source locations in this case we use a sequential approach as opposed to the double difference misfit used for the active case. In this approach the final inverted baseline model is used as the initial guess for carrying out FWI of the monitor dataset. The resulting baseline anomaly and time-lapse change calculated from earthquake data are depicted in Figures 10 (d-f) and 11 (d-f), respectively. We are able to decipher the drop in P-wave velocity caused by the injection of CO_2. Now we try to evaluate the performance of FWI in presence of noise, where we add random Gaussian noise to result in a datasets with a signal to noise ratio (SNR) of 5 dB. The FWI results obtained from inversion of noisy earthquake datasets for the basline and time-lapse inversions are shown in Figures 10 (g-i) and 11 (g-i), respectively. Our results show that despite the adverse effects of the random noise at the current noise level we can still decipher the low-velocity anomaly induced by CO_2 injection. For increased noise levels more robust FWI implementations can be used to overcome the challenge.

The magnitudes of the microseismic events range between 0.3 to 1, and are randomly distributed in all directions at the reservoir depth-level ranging from 1.5 to 2 km as opposed to a directional bias associated with earthquake locations. This leads to a more diverse raypath coverage in comparison to the earthquake scenario. Baseline and monitor events in this case refer to microseismic events that occur when CO_2 is introduced into the subsurface. Similar to the earthquake-scenario we employ a sequential baseline-monitor FWI strategy for inverting the monitor dataset. Inverted baseline anomaly

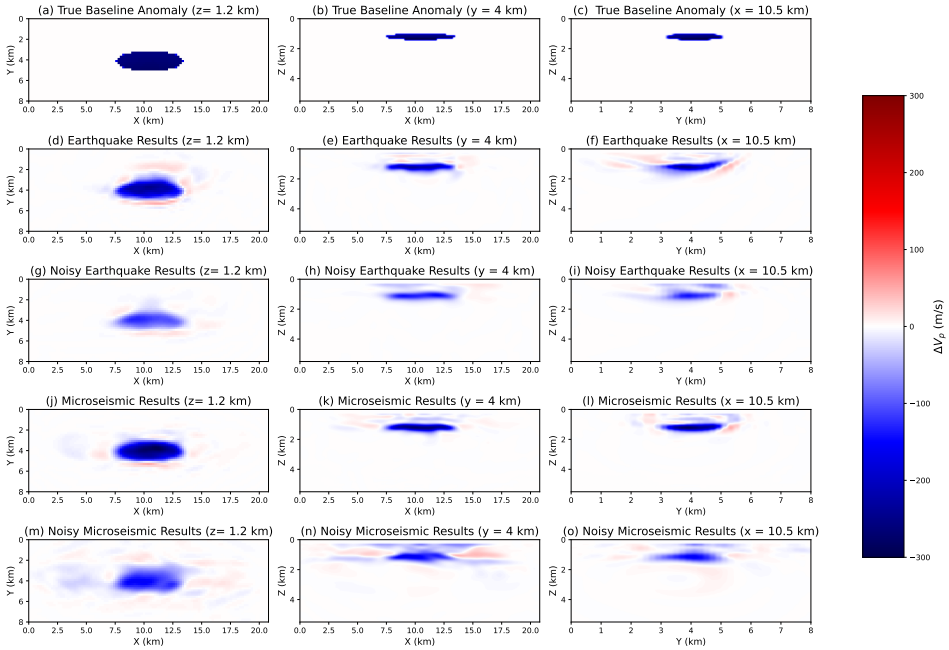

Figure 10. Ground truth for the true (a-c) baseline anomaly. Inverted 2D slices of baseline anomaly inverted from FWI of earthquake (d-f) and microseismic data (j-l). Baseline inversion results obtained from noisy earthquake (g-i) and microseismic datasets (m-o).

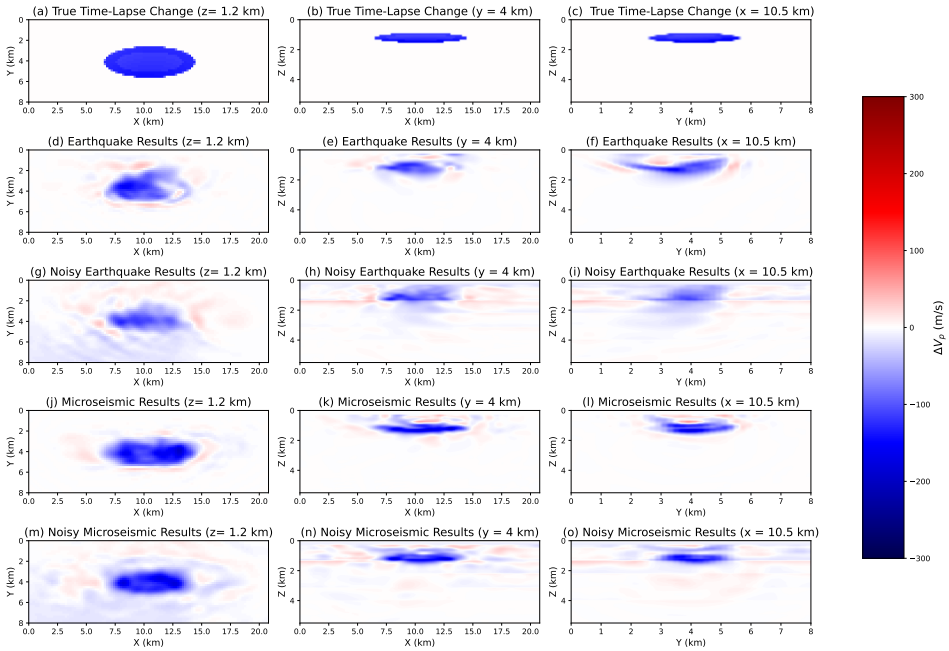

Figure 11. Ground truth for the true (a-c) time-lapse changes. Inverted 2D slices of the time-lapse change estimated from FWI of earthquake (d-f) and microseismic data (j-l). Time-lapse inversion results calculated from noisy earthquake (g-i) and microseismic datasets (m-o).

and time-lapse change models in Figures 10 (j-l) and 11 (j-l) highlight the low-velocity drop created during the two stages of the injection.

Analogous to the earthquake case we also ran a noise-sensitivity test for microseismic inversion with the a SNR of 5 dB. The inverted baseline and time-lapse results derived from noisy microseismic data shown in Figures 10 (m-o) and Figures 11 (m-o) are affected by the added noise, but we can still manage to locate the subsurface changes fairly accurately.

On observing the results derived from the earthquake and microseismic events, we can see that the inverted anomalies from microseismic events are better resolved in comparison to the inverted perturbations from the earthquakes. This is even more evident when we compare the noisy counterparts of the earthquake and microseismic inversion results. The aforementioned diversity of raypaths available for microseismic events leads to a better delineation of the baseline anomaly and the time-lapse changes relative to the subsurface images obtained from the earthquake dataset.

We also examine the data residuals for the four sets of time-lapse inversions corresponding to noisy and noise-free earthquake and microseismic datasets. We select two events each for microseismic and the earthquake scenarios and analyze the data residuals for the central DAS cables. The selected events and the recording DAS cable are highlighted for the earthquake and microseismic events in Figures 12a and 13a, respectively.

Figure 12 show the data residuals for noisy and noise-free earthquake datasets. FWI is fairly robust to the current noise level as seen by the model domain reconstructions and the data residual, coherent arrivals are well explained despite the addition of noise. Similar observations can be made from the data-domain residuals for the microseismic datasets shown in Figure 13.

4 Discussion

We show that time-lapse imaging using active seismic in an offshore setting is capable of producing highly detailed images of the CO_2 plume in the subsurface as shown by the example. Our results show that offshore DAS is a reliable alternative to conventional OBC/OBN sensors. A DAS based acquisition setup can be low-cost, environmentally adaptable and provides enhanced spatial coverage in comparison to conventional seismic sensors (Gorshkov et al., 2022). Active seismic surveys can be repeated more reliably than passive datasets, but they are expensive, difficult to carry out, and can be environmentally invasive.

To overcome the challenges of active seismic surveys, we can use passive data recorded by DAS sensors to image the subsurface. Our results show that it is possible to extract useful information about the CO_2 plume using natural events such as earthquakes and microseismic activity caused by the injection of the greenhouse gas. However, because the occurrence of these events is random in nature, the time-lapse dataset we assemble has poor repeatability. Another thing to keep in mind is that earthquakes are usually spaced sparsely in time so the inversion result is representative of average subsurface CO_2 distribution during this time interval. Despite these shortcomings FWI inverted time-lapse estimates from microseismic and earthquake events provides useful information regarding the subsurface changes with time.

By design, CCS sites are selected in areas of low seismicity, the Pelican site is no exception. Earthquakes are less likely to occur in the area as seismicity of the region was studied before selection of Pelican field as a storage site. A baseline passive seismic monitoring study (Attanayake et al., 2023) of the area revealed that no seismic activity was recorded within a 10 km radius of the site. Microseismic events are more likely to be recorded

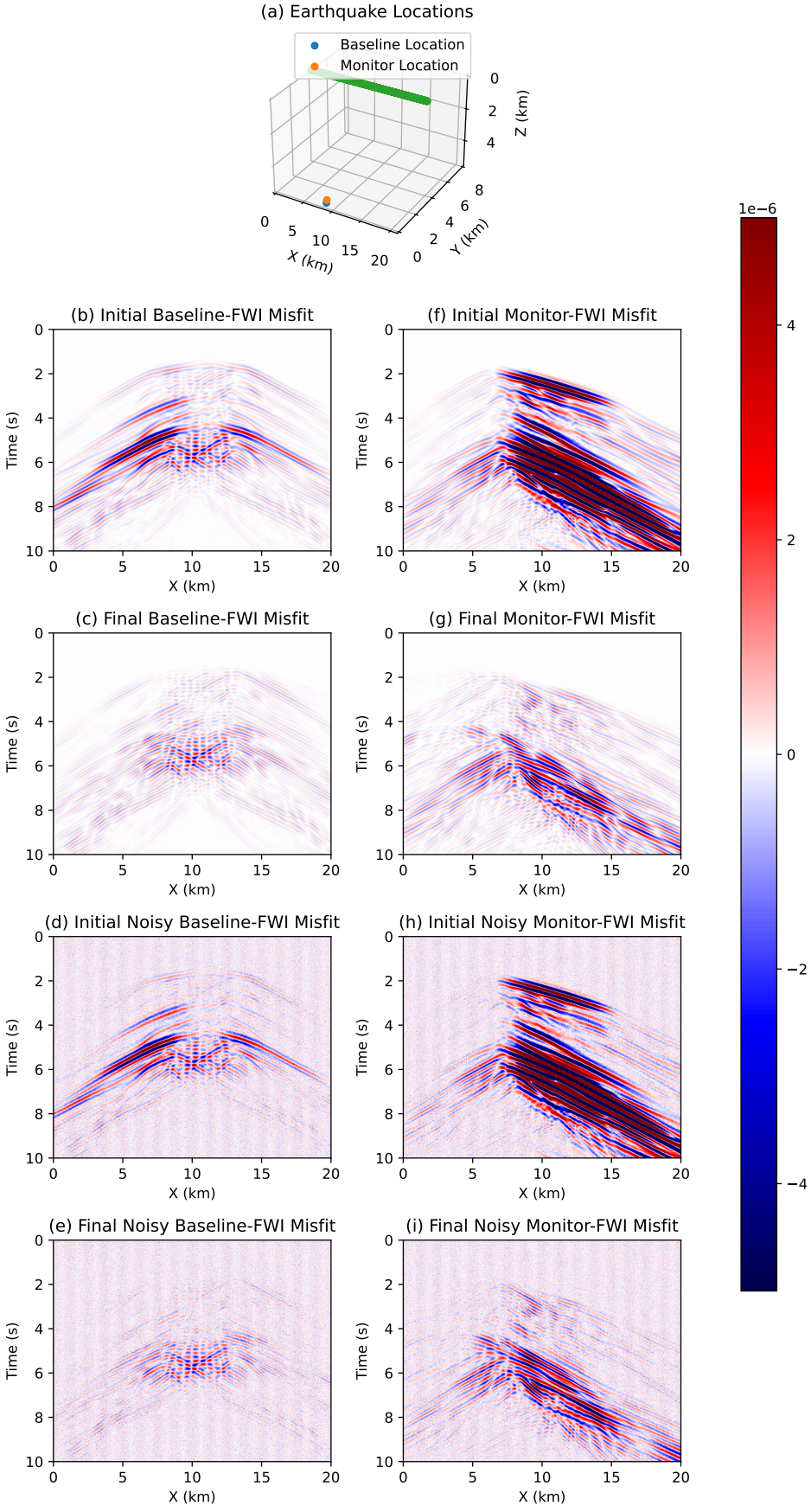

Figure 12. Baseline initial and final data residuals for clean (a-b) and noisy earthquake data(c-d), followed by selected initial and final monitor data residuals (e-h).

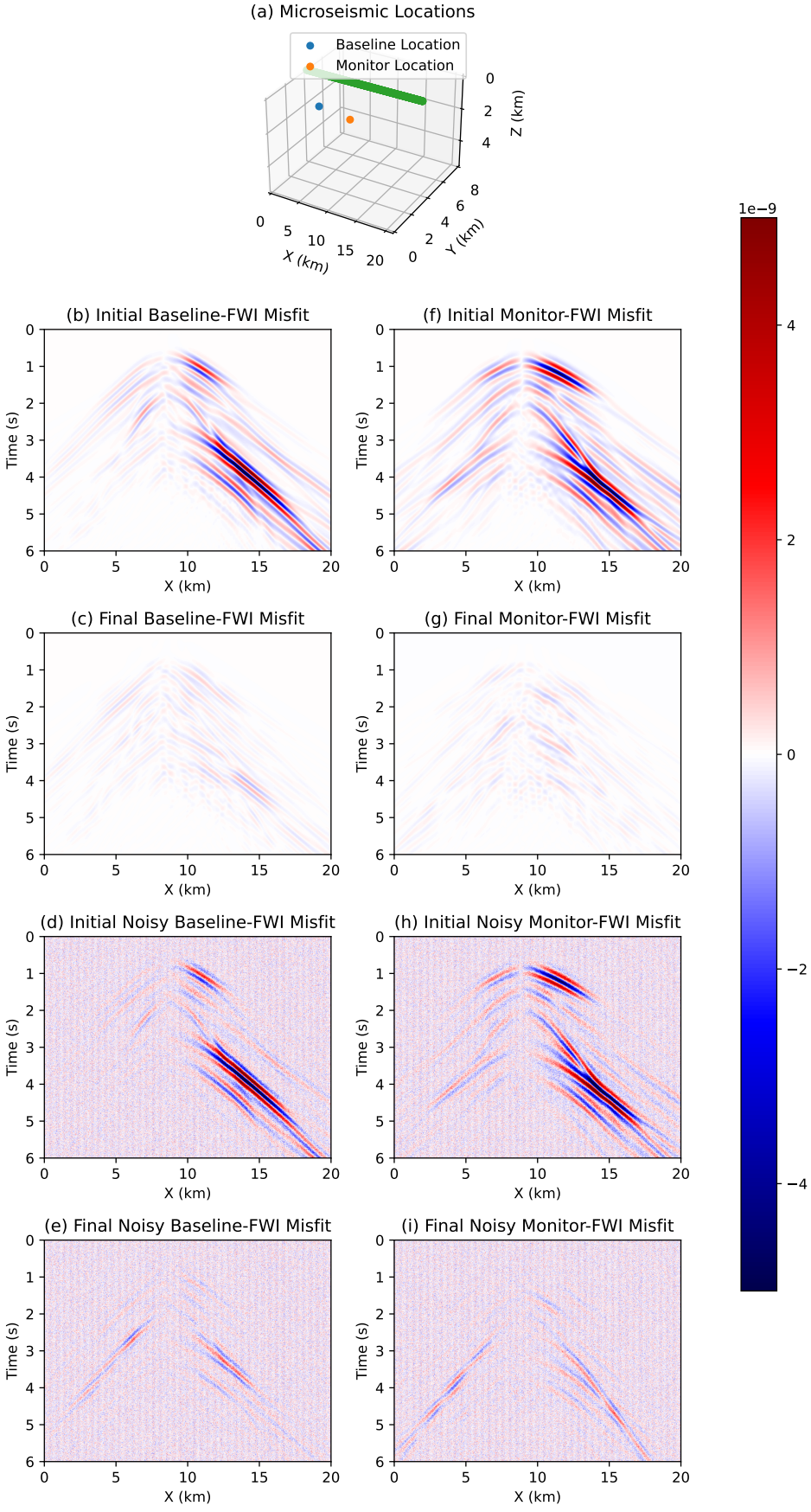

Figure 13. Baseline initial and final data residuals for clean (a-b) and noisy microseismic data(c-d), followed by selected initial and final monitor data residuals (e-h).

when a fluid is injected into an underground reservoir. Around 1500 microseismic events were detected in a space of three years at the In Salah storage site in Algeria, and these occurrences coincided with increased injection rates (Oye et al., 2013). Glubokovskikh et al. (2022) reported that low-pressure injection of CO_2 managed to induce detectable microseismic events of M_w 0.5 in the Otway project, Australia. A small fault was reactivated as the CO_2 plume passed through it, causing these events. Inaccuracies in locating the microseismic hypocentres and earthquake epicentres in relation to depth uncertainties will effect the FWI imaging negatively. One can overcome that by incorporating the source location into the FWI framework. Also, especially for microseismic events additional information in the form of borehole DAS would aid in narrowing down on the depth uncertainty of the microseismic hypocentre (Jones et al., 2014).

Virtual shot data derived from ambient noise cross-correlations of passive data can be beneficial for monitoring the shallow subsurface for any potential leakages. Ambient noise based shot gathers are rich in surface waves and these events are mostly sensitive to shallow S-wave velocity structure. We exploit this feature to detect any shallow leakages in the example. Figure 7 shows an observable shift of the observed dispersion curve (green) towards lower velocities in comparison to the dispersion curve corresponding to the pre-injection shallow subsurface (red). This serves as a clear indicator of low-velocity anomaly, which could be potentially be turned into a early-warning system for detection of potential leakages.

All numerical examples in the study assume perfect coupling between the sea-floor and the optical fibre. But in practice uneven coupling can persist across the DAS cable arising from the undulating bathymetry leading to suspended cables in certain portions of the optical fibre cable (Celli et al., 2023). These variations can cause distortions which lead to recorded data with poor SNR. These discrepancies can be mitigated by burying the cable a few meters below the sea-floor as done by Shinohara et al. (2022). Another way to handle these distortions is by applying robust imaging methods which focus on the kinematic or phase information stored in the waveforms, such as the traveltimes and phase dispersion phenomena. WD method is used here is to overcome the reliance on absolute amplitudes in the observed data and mitigating the effect of distortions on the inverted results. The acquisition geometry setup of the DAS cables is pivotal in monitoring of the plume. Due to the broadside limitation of conventional DAS the measurements are sensitive to waves propagating along the cable, so for a horizontal cable lying on the sea-floor most of the information of the CO_2 plume comes from diving or refracted events and wide-angle reflections. This may lead to poor detection of smaller CO_2 anomalies. There have been recent advances to overcome this limitation by utilising helical fibres which are able to sense a diverse range of arrivals (Kuvshinov, 2016).

5 Conclusions

We have developed a multifaceted monitoring workflow for CCS by combining passive and active DAS data with wave equation imaging methods. We first validated that the simulated DAS measurements can provide equivalent results to conventional geophones by means of synthetic comparison. Then, we established that even with poor repeatability we can salvage sensible time-lapse estimates from passive data. By circumventing the need for an active survey, we can reduce the monitoring costs and the associated environmental footprint. Additionally, we have shown that the WD method can be used to identify potential leaks in the shallow subsurface. Based on our results we recommend a hierarchical approach to provide the most cost-efficient and lowest environmental footprint solution for monitoring CO_2 in the subsurface. The passive datasets recorded using DAS can serve as an early warning trigger should an unexpected change be detected. This will then inform a more detailed monitoring response using targeted active seismic surveys to further refine the timelapse estimate.

Open Research Section

The velocity models and well data used for this study can be downloaded from National Offshore Petroleum Titled Administrator website (`https://nopims.dmp.wa.gov.au/nopims`) under the survey named Pelican 3D MSS (CarbonNet) 2018. All time-lapse imaging synthetics were run on Salvus (Afanasiev et al., 2018). The notebooks used for generating the synthetic datasets and their corresponding inversions are provided here `https://doi.org/10.5281/zenodo.10584281`. The velocity model used for generating the synthetics is also shared on the aforementioned link.

Acknowledgments

This research was fully funded by the Deep Earth Imaging Future Science Platform, CSIRO. We are grateful to CSIRO HPC for providing us with access to their HPC resources for this project. This work was also supported by resources provided by the Pawsey Supercomputing Research Centre with funding from the Australian Government and the Government of Western Australia. The Carbonnet project team are thanked for the provision of 3D velocity models. We also acknowledge their thoughtful comments on the results of the study.

References

Afanasiev, M., Boehm, C., van Driel, M., Krischer, L., Rietmann, M., May, D. A., ... Fichtner, A. (2018, 11). Modular and flexible spectral-element waveform modelling in two and three dimensions. *Geophysical Journal International*, *216*(3), 1675-1692. Retrieved from `https://doi.org/10.1093/gji/ggy469` doi: 10.1093/gji/ggy469

Ajo-Franklin, J. B., Dou, S., Lindsey, N. J., Monga, I., Tracy, C., Robertson, M., ... Li, X. (2019, Feb 04). Distributed acoustic sensing using dark fiber for near-surface characterization and broadband seismic event detection. *Scientific Reports*, *9*(1), 1328. Retrieved from `https://doi.org/10.1038/s41598-018-36675-8` doi: 10.1038/s41598-018-36675-8

Attanayake, J., Jones, A., Gibson, G., & Sandiford, M. (2023). Pre-commercial baseline passive seismic monitoring around carbonnet's pelican site in the offshore gippsland basin, victoria—the first five years. *International Journal of Greenhouse Gas Control*, *128*, 103962. Retrieved from `https://www.sciencedirect.com/science/article/pii/S1750583623001329` doi: https://doi.org/10.1016/j.ijggc.2023.103962

Bensen, G. D., Ritzwoller, M. H., Barmin, M. P., Levshin, A. L., Lin, F., Moschetti, M. P., ... Yang, Y. (2007, 06). Processing seismic ambient noise data to obtain reliable broad-band surface wave dispersion measurements. *Geophysical Journal International*, *169*(3), 1239-1260. Retrieved from `https://doi.org/10.1111/j.1365-246X.2007.03374.x` doi: 10.1111/j.1365-246X.2007.03374.x

Celli, N. L., Bean, C. J., & O'Brien, G. S. (2023, 11). Full-waveform simulation of DAS records, response and cable-ground coupling. *Geophysical Journal International*, *236*(1), 659-674. Retrieved from `https://doi.org/10.1093/gji/ggad449` doi: 10.1093/gji/ggad449

Chadwick, R. A., & Noy, D. J. (2015). Underground co2 storage: demonstrating regulatory conformance by convergence of history-matched modeled and observed co2 plume behavior using sleipner time-lapse seismics. *Greenhouse Gases: Science and Technology*, *5*(3), 305-322. Retrieved from `https://onlinelibrary.wiley.com/doi/abs/10.1002/ghg.1488` doi: https://doi.org/10.1002/ghg.1488

Chen, Y., & Saygin, E. (2022). 3-d s wave imaging via robust neural network interpolation of 2-d profiles from wave-equation dispersion inversion of seis-

mic ambient noise. *Journal of Geophysical Research: Solid Earth*, *127*(12), e2022JB024663. Retrieved from https://agupubs.onlinelibrary.wiley.com/doi/abs/10.1029/2022JB024663 (e2022JB024663 2022JB024663) doi: https://doi.org/10.1029/2022JB024663

Eaid, M. V., Keating, S. D., & Innanen, K. A. (2020). Multiparameter seismic elastic full-waveform inversion with combined geophone and shaped fiber-optic cable data. *GEOPHYSICS*, *85*(6), R537-R552. Retrieved from https://doi.org/10.1190/geo2020-0170.1 doi: 10.1190/geo2020-0170.1

Furre, A.-K., Eiken, O., Alnes, H., Vevatne, J. N., & Kiær, A. F. (2017). 20 years of monitoring co2-injection at sleipner. *Energy Procedia*, *114*, 3916-3926. Retrieved from https://www.sciencedirect.com/science/article/pii/S1876610217317174 (13th International Conference on Greenhouse Gas Control Technologies, GHGT-13, 14-18 November 2016, Lausanne, Switzerland) doi: https://doi.org/10.1016/j.egypro.2017.03.1523

Glubokovskikh, S., Pevzner, R., Dance, T., Caspari, E., Popik, D., Shulakova, V., & Gurevich, B. (2016). Seismic monitoring of co2 geosequestration: Co2crc otway case study using full 4d fdtd approach. *International Journal of Greenhouse Gas Control*, *49*, 201-216. Retrieved from https://www.sciencedirect.com/science/article/pii/S1750583616300809 doi: https://doi.org/10.1016/j.ijggc.2016.02.022

Glubokovskikh, S., Saygin, E., Shapiro, S., Gurevich, B., Isaenkov, R., Lumley, D., ... Pevzner, R. (2022). A small co2 leakage may induce seismicity on a sub-seismic fault in a good-porosity clastic saline aquifer. *Geophysical Research Letters*, *49*(12), e2022GL098062. Retrieved from https://agupubs.onlinelibrary.wiley.com/doi/abs/10.1029/2022GL098062 (e2022GL098062 2022GL098062) doi: https://doi.org/10.1029/2022GL098062

Gorshkov, B. G., Yüksel, K., Fotiadi, A. A., Wuilpart, M., Korobko, D. A., Zhirnov, A. A., ... Lobach, I. A. (2022). Scientific applications of distributed acoustic sensing: State-of-the-art review and perspective. *Sensors*, *22*(3). Retrieved from https://www.mdpi.com/1424-8220/22/3/1033 doi: 10.3390/s22031033

Harvey, S., Hopkins, J., Kuehl, H., O'Brien, S., & Mateeva, A. (2022). Quest ccs facility: Time-lapse seismic campaigns. *International Journal of Greenhouse Gas Control*, *117*, 103665. Retrieved from https://www.sciencedirect.com/science/article/pii/S1750583622000834 doi: https://doi.org/10.1016/j.ijggc.2022.103665

Hoffman, N. (2018). The carbonnet project's pelican storage site in the gippsland basin. *14th Greenhouse Gas Control Technologies Conference Melbourne 21-26 October 2018 (GHGT-14)*. Retrieved from https://ssrn.com/abstract=3366069

Hoult, R., Pascale, A., Jones, A., & Allen, T. (2021, 11). The mw 5.9 woods point earthquake: A preliminary investigation of the ground motion observations..

IEA. (2021). IEA net zero by 2050 report. *IPCC AR6 Report*. Retrieved from https://www.ipcc.ch/report/sixth-assessment-report-cycle/

Jenkins, C., Chadwick, A., & Hovorka, S. D. (2015). The state of the art in monitoring and verification—ten years on. *International Journal of Greenhouse Gas Control*, *40*, 312-349. Retrieved from https://www.sciencedirect.com/science/article/pii/S1750583615001723 (Special Issue commemorating the 10th year anniversary of the publication of the Intergovernmental Panel on Climate Change Special Report on CO2 Capture and Storage) doi: https://doi.org/10.1016/j.ijggc.2015.05.009

Jones, G., Kendall, J.-M., Bastow, I., & Raymer, D. (2014). Locating microseismic events using borehole data. *Geophysical Prospecting*, *62*(1), 34-49. Retrieved from https://onlinelibrary.wiley.com/doi/abs/10.1111/1365-2478.12076 doi: https://doi.org/10.1111/1365-2478.12076

Kamei, R., Nakata, N., & Lumley, D. (2015, 08). Introduction to microseismic source mechanisms. *The Leading Edge*, *34*(8), 876-880. Retrieved from https://doi.org/10.1190/tle34080876.1 doi: 10.1190/tle34080876.1

Kuvshinov, B. (2016). Interaction of helically wound fibre-optic cables with plane seismic waves [Journal Article]. *Geophysical Prospecting*, *64*(3), 671-688. Retrieved from https://www.earthdoc.org/content/journals/10.1111/1365-2478.12303 doi: https://doi.org/10.1111/1365-2478.12303

Li, J., Feng, Z., & Schuster, G. (2016, 12). Wave-equation dispersion inversion. *Geophysical Journal International*, *208*(3), 1567-1578. Retrieved from https://doi.org/10.1093/gji/ggw465 doi: 10.1093/gji/ggw465

Lindsey, N. J., & Martin, E. R. (2021). Fiber-optic seismology. *Annual Review of Earth and Planetary Sciences*, *49*(1), 309-336. Retrieved from https://doi.org/10.1146/annurev-earth-072420-065213 doi: 10.1146/annurev-earth-072420-065213

Lindsey, N. J., Martin, E. R., Dreger, D. S., Freifeld, B., Cole, S., James, S. R., ... Ajo-Franklin, J. B. (2017). Fiber-optic network observations of earthquake wavefields. *Geophysical Research Letters*, *44*(23), 11,792-11,799. Retrieved from https://agupubs.onlinelibrary.wiley.com/doi/abs/10.1002/2017GL075722 doi: https://doi.org/10.1002/2017GL075722

Liu, H., Li, J., & Wang, Y. (2022). Wave equation dispersion inversion of distributed acoustic sensing data. *Journal of Geophysical Research: Solid Earth*, *127*(11), e2022JB024671. Retrieved from https://agupubs.onlinelibrary.wiley.com/doi/abs/10.1029/2022JB024671 (e2022JB024671 2022JB024671) doi: https://doi.org/10.1029/2022JB024671

Mora, P. (1987). Nonlinear two-dimensional elastic inversion of multioffset seismic data. *GEOPHYSICS*, *52*(9), 1211-1228. Retrieved from https://doi.org/10.1190/1.1442384 doi: 10.1190/1.1442384

Nocedal, J., & Wright, S. (2006). *Numerical optimization* (2. ed. ed.). New York, NY: Springer.

Oye, V., Aker, E., Daley, T. M., Kühn, D., Bohloli, B., & Korneev, V. (2013). Microseismic monitoring and interpretation of injection data from the in salah co2 storage site (krechba), algeria. *Energy Procedia*, *37*, 4191-4198. Retrieved from https://www.sciencedirect.com/science/article/pii/S187661021300564X (GHGT-11 Proceedings of the 11th International Conference on Greenhouse Gas Control Technologies, 18-22 November 2012, Kyoto, Japan) doi: https://doi.org/10.1016/j.egypro.2013.06.321

Plessix, R.-E. (2006, 11). A review of the adjoint-state method for computing the gradient of a functional with geophysical applications. *Geophysical Journal International*, *167*(2), 495-503. Retrieved from https://doi.org/10.1111/j.1365-246X.2006.02978.x doi: 10.1111/j.1365-246X.2006.02978.x

Shinohara, M., Yamada, T., Akuhara, T., Mochizuki, K., & Sakai, S. (2022). Performance of seismic observation by distributed acoustic sensing technology using a seafloor cable off sanriku, japan. *Frontiers in Marine Science*, *9*. Retrieved from https://www.frontiersin.org/articles/10.3389/fmars.2022.844506 doi: 10.3389/fmars.2022.844506

Tarantola, A. (1986). A strategy for nonlinear elastic inversion of seismic reflection data. *GEOPHYSICS*, *51*(10), 1893-1903. Retrieved from https://doi.org/10.1190/1.1442046 doi: 10.1190/1.1442046

Tsuji, T., Ikeda, T., Matsuura, R., Mukumoto, K., Hutapea, F. L., Kimura, T., ... Shinohara, M. (2021, Sep 27). Continuous monitoring system for safe managements of co2 storage and geothermal reservoirs. *Scientific Reports*, *11*(1), 19120. Retrieved from https://doi.org/10.1038/s41598-021-97881-5 doi: 10.1038/s41598-021-97881-5

Urosevic, M., Pevzner, R., Shulakova, V., Kepic, A., Caspari, E., & Sharma, S. (2011). Seismic monitoring of co2 injection into a depleted gas reser-

voir–otway basin pilot project, australia. *Energy Procedia*, *4*, 3550-3557. Retrieved from https://www.sciencedirect.com/science/article/pii/S1876610211004802 (10th International Conference on Greenhouse Gas Control Technologies) doi: https://doi.org/10.1016/j.egypro.2011.02.283

Williams, E. F., Fernández-Ruiz, M. R., Magalhaes, R., Vanthillo, R., Zhan, Z., González-Herráez, M., & Martins, H. F. (2021). Scholte wave inversion and passive source imaging with ocean-bottom das. *The Leading Edge*, *40*(8), 576-583. Retrieved from https://doi.org/10.1190/tle40080576.1 doi: 10.1190/tle40080576.1

Yang, D., Liu, F., Morton, S., Malcolm, A., & Fehler, M. (2016). Time-lapse full-waveform inversion with ocean-bottom-cable data: Application on valhall field. *GEOPHYSICS*, *81*(4), R225-R235. Retrieved from https://doi.org/10.1190/geo2015-0345.1 doi: 10.1190/geo2015-0345.1

Yust, M. B. S., Cox, B. R., Vantassel, J. P., Hubbard, P. G., Boehm, C., & Krischer, L. (2023, Feb). Near-surface 2d imaging via fwi of das data: An examination on the impacts of fwi starting model. *Geosciences*, *13*(3), 63. Retrieved from http://dx.doi.org/10.3390/geosciences13030063 doi: 10.3390/geosciences13030063